ROYAL SOCIETY
OF CHEMISTRY

PAPER
Chao Liu, Kaicheng Zhang, Christoph J. Brabec *et al.*
A simultaneous synergistic protection mechanism in hybrid perovskite–organic multi-junctions enables long-term stable and efficient tandem solar cells

Check for updates

A simultaneous synergistic protection mechanism in hybrid perovskite–organic multi-junctions enables long-term stable and efficient tandem solar cells

Chao Liu, [†*ab] Kaicheng Zhang,[†*b] Xin Zhou,[d] Mingjian Wu, [d] Paul Weitz,[b] Shudi Qiu, [b] Andrej Vincze, [e] Yuchen Bai,[b] Michael A. Anderson,[fg] Johannes Frisch,[fg] Regan G. Wilks, [fg] Marcus Bär, [afgl] Zijian Peng, [bi] Chaohui Li, [bi] Jingjing Tian,[bi] Jiyun Zhang, [b] Jianchang Wu,[a] Jonas Englhard,[h] Thomas Heumüller, [ab] Jens Hauch,[a] Yixing Huang,[j] Ning Li, [ak] Julien Bachmann, [h] Erdmann Spiecker [d] and Christoph J. Brabec*[abc]

Perovskite–organic tandem solar cells (P–O TSCs) hold great promise for next-generation thin-film photovoltaics, with steadily improving power conversion efficiency (PCE). However, the development of optimal interconnecting layers (ICLs) remains one major challenge for further efficiency gains, and progress in understanding the improved long-term stability of P–O tandem configuration has been lagging. In this study, we experimentally investigate the enhanced stability of p–i–n P–O TSCs employing a simplified C_{60}/atomic-layer-deposition (ALD) SnO_x/PEDOT:PSS ICL without an additional charge recombination layer (CRL), which achieve an averaged efficiency of 25.12% and a hero efficiency of 25.5%. Our finding discovers that the recrystallization of C_{60}, a widely used electron transport layer in perovskite photovoltaics, leads to the formation of grain boundaries during operation, which act as preferential migration channels for the interdiffusion of halide and Ag ions. Critically, we demonstrate for the first time that the tandem device architecture, incorporating organic semiconductor layers, effectively suppresses the bi-directional ion diffusion and mitigates electrode corrosion. Thus, the P–O TSC establishes a mutual protection system: the organic layers stabilize the perovskite sub-cell by suppressing ion diffusion-induced degradation, and the perovskite layer shields the organic sub-cell from spectrally induced degradation. The simultaneous synergistic protection mechanism enables P–O TSCs to achieve exceptional long-term operational stability, retaining over 91% of their initial efficiency after 1000 hours of continuous metal–halide lamp illumination, and to exhibit minimal fatigue after 86 cycles (2067 hours) of long-term diurnal (12/12-hour) testing. These results demonstrate that tandem cells significantly outperform their single-junction counterparts in both efficiency and stability.

[a] *Helmholtz-Institute Erlangen-Nürnberg for Renewable Energy (HI ERN), Immerwahrstraße 2, 91058 Erlangen, Germany. E-mail: c.liu@fz-juelich.de, christoph.brabec@fau.de*

[b] *Institute of Materials for Electronics and Energy Technology (i-MEET), Friedrich-Alexander-Universität Erlangen-Nürnberg (FAU), Martensstr. 7, 91058 Erlangen, Germany. E-mail: kaichengzhang@zoho.com*

[c] *Institute of Energy Materials and Devices (IMD-3), Forschungszentrum Jülich GmbH, Wilhelm-Johnen-Straße 52428, Jülich, Germany*

[d] *Institute of Micro- and Nanostructure Research & Center for Nanoanalysis and Electron Microscopy (CENEM), Friedrich-Alexander-Universität Erlangen-Nürnberg (FAU), IZNF, Cauerstr. 3, 91058 Erlangen, Germany*

[e] *International Laser Centre SCSTI, 84104 Bratislava, Slovak Republic*

[f] *Department Interface Design, Helmholtz-Zentrum Berlin für Materialien und Energie GmbH (HZB), Albert-Einstein-Str. 15, 12489 Berlin, Germany*

[g] *Energy Materials In situ Laboratory Berlin (EMIL), Helmholtz-Zentrum Berlin für Materialien und Energie GmbH (HZB), Albert-Einstein-Str. 15, 12489 Berlin, Germany*

[h] *Chemistry of Thin Film Materials, Materials Chemistry section, Department of Chemistry and Pharmacy, Friedrich-Alexander-Universität Erlangen-Nürnberg (FAU), IZNF, Cauerstr. 3, 91058 Erlangen, Germany*

[i] *Erlangen Graduate School in Advanced Optical Technologies (SAOT), Paul-Gordan-Straße 6, 91052 Erlangen, Germany*

[j] *Institute of Medical Technology, Health Science Center, Peking University, Xueyuan Rd. 38, Haidian District, Beijing, 100083, China*

[k] *Institute of Polymer Optoelectronic Materials & Devices, Guangdong Basic Research Center of Excellence for Energy & Information Polymer Materials, State Key Laboratory of Luminescent Materials & Devices, South China University of Technology, Guangzhou, 510640, P. R. China*

[l] *Department of Chemistry and Pharmacy, Friedrich-Alexander-Universität Erlangen-Nürnberg (FAU), Egerlandstr. 3, 91058 Erlangen, Germany*

† These authors contributed equally: Chao Liu, Kaicheng Zhang.

This journal is © The Royal Society of Chemistry 2026

Energy Environ. Sci., 2026, **19**, 1137–1147 | **1137**

Broader context

Monolithic perovskite/organic tandem solar cells (P–O TSCs) have drawn considerable attention due to their potential to surpass the Shockley–Queisser limit. While recent advances have demonstrated steady improvements in efficiency, challenges in interconnecting layer (ICL) design and limited understanding of operational stability remain major barriers toward commercialization. Here, we present a simplified ICL architecture without an additional charge recombination layer, enabling a champion efficiency of 25.5%. Beyond that, we experimentally demonstrate that the perovskite sub-cell functions as a robust optical filter, shielding the organic sub-cell from light-induced degradation. Uniquely, the organic layer is revealed to effectively suppress ion migration from the perovskite layer, thereby establishing a synergistic protection mechanism within the P–O tandem configuration that ensures exceptional long-term stability. P–O TSCs exhibit clear advantages over their single-junction counterparts in both efficiency and lifetime. Our findings underscore the promise of P–O TSCs as a viable route toward high-efficiency, stable, and sustainable photovoltaic technologies.

Introduction

Tandem solar cells (TSCs), integrating both wide and narrow bandgap (NBG) photo absorbers with complementary absorption spectra, have ignited tremendous interest, offering the potential to surpass the Shockley–Queisser (S–Q) limit.[1–3] Halide perovskite materials, featured with a broad bandgap (E_g) tunability, render them excellent building blocks as both front and rear sub-cells in TSCs.[4,5] Recently, perovskite-based TSCs have reached certified power conversion efficiencies (PCEs) of 34.6% and 30.1% for perovskite-silicon TSCs and monolithic all-perovskite TSCs, respectively,[6,7] much higher than the current record PCE of single-junction perovskite devices (26.95%).[6] On the downside, the silicon cells are usually fabricated at high temperatures exceeding 400 °C, while the NBG Sn-based perovskites ($E_g < 1.4$ eV) in all-perovskite tandem devices encounter the intractable oxidation of Sn^{2+} to Sn^{4+}, triggering undesirable heavy p-type doping or device degradation.[8–10] Alternatively, the advent of non-fullerene acceptors (NFAs), featuring near-infrared-region absorption, non-toxicity, and orthogonal solution processibility at low-temperatures as well as a simple fabrication process, has ignited the vigorous performance progress of organic solar cells (OSCs) over 20%, which positions them as viable rear NBG sub-cell candidates for perovskite-based TSCs.[11,12] Accordingly, perovskite–organic TSCs (P–O TSCs), which combine organic and halide perovskite semiconductors, are expected to yield high open-circuit voltage (V_{oc}), and to optimize sunlight utilization, especially anticipating new generations of high performing low bandgap NFAs with $E_g < 1.2$ eV. The efficiencies of P–O TSCs have been improved rapidly, now achieving 26.7% (certified 26.4%).[13] Despite these achievements, developing efficient monolithic P–O TSCs still faces significant challenges, particularly in further improving both efficiency and stability. Progress in these areas hinges on meticulous fabrication of each component, including high-quality wide bandgap (WBG) halide perovskite front sub-cells, robust and efficient interconnecting layers (ICLs), and optimized organic rear sub-cells with finely tuned morphologies and extended absorption in the near-infrared (NIR) range.[14–19] The ICLs, which electrically stack front and rear sub-cells in series, play a pivotal role in determining the overall performance of TSCs by influencing internal electrical contact and energy alignment, managing light utilization in rear sub-cells, and governing charge collection and recombination between the sub-cells. Therefore, the design of

ideal ICLs must ensure good quasi-ohmic contact, efficient internal charge recombination, minimized electrical and optical losses, as well as low manufacturing cost. In state-of-the-art p–i–n P–O TSCs, ICLs are commonly composed of tin oxide (SnO_x) deposited by atomic-layer deposition (ALD) as an electron transporting layer (ETL) and an evaporated thin metal layer (Au or Ag) or a sputtered transparent metal oxide (indium zinc oxide[15] or indium tin oxide[20]) as a charge recombination layer (CRL). The incorporation of an additional CRL serves two critical functions: (1) compensating for insufficient electrical contact between ETL and hole transporting layer to achieve quasi-ohmic behaviour, and (2) offering sufficient charge recombination sites.[14,17,21,22] Unfortunately, the inclusion of thin metal layers as CRLs inevitably leads to light absorption loss in the rear OSC sub-cell due to the metal films' substantial parasitic localized surface plasma resonance absorption and light reflection,[15,18,23] which in turn limits the full advantage of tandem structures. Additionally, metal elements can react with mobile halide species, which can contribute to the deterioration of device stability.[24–26] While highly transparent sputtered metal-oxide layers offer alternatives, the sputtering process risks damaging the underlying layers due to the high-energy ion generated in the sputter proces.[27,28] Furthermore, the incorporation of extra CRLs produced through different methods into prevalent ICLs complicates device fabrication processes and increases manufacturing costs, confining their practical application potential.[14,15,18] These considerations drive the exploration of CRL-free ICL architectures, which are aimed at realizing stable and high-performance hybrid multijunction cells. Preliminary implementations utilizing ALD SnO_x-based, CRL-free ICLs in P–O TSCs achieved only 22.31% efficiency,[29,30] constrained by substantial electrical losses and suboptimal band alignment within the ICL. Crucially, the properties of ALD-grown SnO_x can be finely tuned by modulation of deposition parameters (*e.g.*, reaction time, temperature, and precursor selection[31–33]), offering a viable strategy to establish efficient electrical contacts while eliminating CRLs, thereby enhancing performance of CRL-free P–O tandem architectures.

Besides, a critical, currently underrepresented research aspect is the operational stability of P–O TSCs compared to the involved single-junction cells. While some studies have vaguely demonstrated that the architectural design of P–O tandem devices contributes to enhanced photostability, the mechanisms remain insufficiently addressed.[14,15,18,19] UV-visible light

1138 | *Energy Environ. Sci.*, 2026, **19**, 1137–1147

This journal is © The Royal Society of Chemistry 2026

wavelength-dependent degradation is one of the leading degradation issues for OSCs,[2,34] and recent work has shown that this fundamental degradation can be delayed or even prevented by using filters or light converters in the UV-visible regime.[35,36] Preliminary stability data of P–O TSCs indicate that the bottom WBG inorganic halide perovskite may play a similar protective role for the organic semiconductor materials by blocking harmful UV-visible light, thus contributing to improved operational stability.[2,18,34,35] However, there is a lack of in-depth experimental investigation into how the single-junction sub-cells of multi-junction cells influence each other's stability. Addressing this critical gap in understanding the long-term performance of P–O tandem devices is also a major focused aspect of this paper.

In this work, we present highly efficient and stable P–O TSCs employing a C_{60}/optimized ALD SnO_x/PEDOT:PSS ICL with significantly enhanced recombination efficiency. The key component of the optimized ICL, which eliminates the need of an additional CRL to achieve high transparency and reduced electrical losses, is a modified ALD SnO_x layer that is deposited by sequentially using H_2O and H_2O_2 with high reactivity as oxygen sources. A thin, H_2O-processed ALD SnO_x film is deposited prior to the H_2O_2-converted SnO_x film to protect the underlying films from the damage caused by H_2O_2 vapor. The resulting H_2O-/H_2O_2-processed ALD-SnO_x film exhibits greatly improved electrical properties and forms an excellent quasi-ohmic contact with PEDOT:PSS in comparison to the conventional pure H_2O-processed SnO_x/PEDOT:PSS combination. Accordingly, the optimal ICL displays superb protection capability, effective charge recombination efficiency, and high NIR transmittance, which enables P–O TSCs to achieve an average

efficiency of 25.12%, along with a V_{oc} of 2.11 V and an outstanding short-current density (J_{sc}) of 15.38 mA cm^{-2}. Additionally, we observe that the commonly used C_{60} film undergoes recrystallization over operation time, leading to the formation of structures with grain boundaries, which serve as bi-directional migration channels for halide ions from the adjacent perovskite layer and the top metal Ag electrode. More interestingly, a compelling experimental study demonstrates that integrating the polymer organic layers within the tandem configuration largely suppresses the interdiffusion of mobile ions and prevents electrode corrosion. This integration establishes a mutual stabilization mechanism between the two single-junction sub-cells of the tandem configuration: the capping polymer organic sub-cell effectively suppresses ion-induced degradation, while the halide perovskite layer protects the organic absorber layer from the spectrally induced degradation. As a result, our target P–O TSCs show distinguished operational photostability, retaining 91.68% of initial efficiency after 1000 hours of continuous exposure to metal halide lamp (MHL) without any UV filter, which is significantly more stable than these single-junction counterparts. Moreover, these P–O TSCs exhibit extraordinary anti-fatigue behavior after a prolonged diurnal (12/12-hour) cycle test for 2067 hours.

Characterization of ALD SnO_x films with different reactants and device performance

Fig. 1a illustrates the schematics of the ALD process (details are described in the SI). The experimental details of the ALD process based on H_2O and H_2O_2 are schematically depicted in Scheme S1. Different oxygen reactants have varying reactivities, which determine the electronic properties of the SnO_x layer.[33,37]
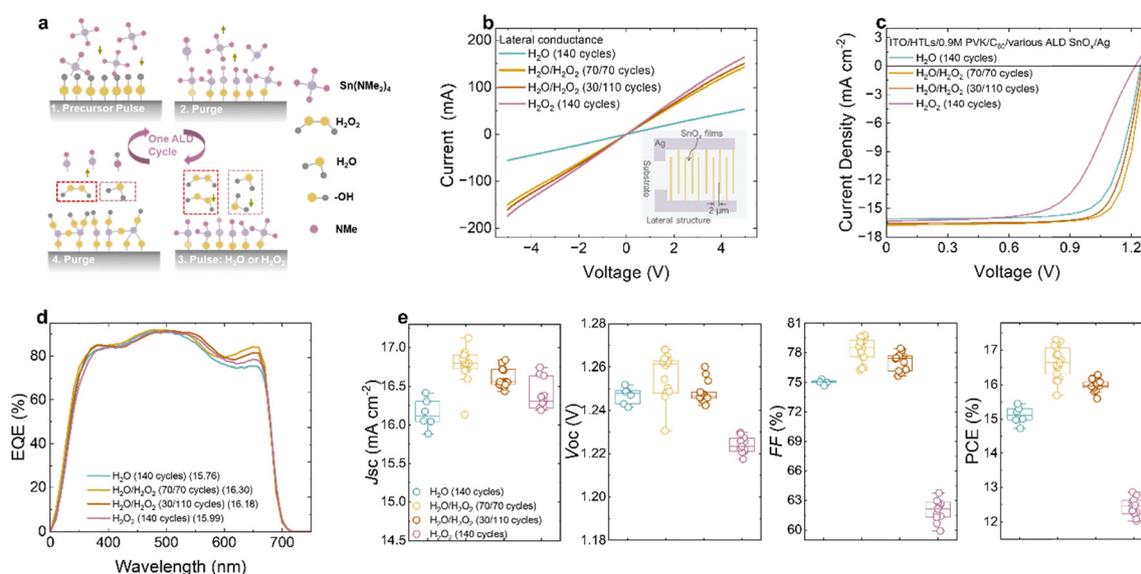

Fig. 1 Photovoltaic characteristics of SPVKs based on ALD SnO_x processed from H_2O, H_2O/H_2O_2, and H_2O_2 reactants, respectively. (a) Schematic diagram of the ALD process, including precursor, reactant source pulse, and inert gas purge.[41] (b) The lateral conductance measurements in a structure consisting of interdigitated Ag/SnO_x films/interdigitated Ag. The inserted picture shows schematic diagram of the interdigitated finger electrode. (c)–(e) J–V curves measured with a reverse scanning direction, EQE spectra, and statistical performance (J_{sc}, V_{oc}, FF, PCE) of SPVKs based on various ALD SnO_x films, respectively.

Initially, the electrical properties of ALD-processed SnO_x films with pure H_2O, H_2O_2, and H_2O/H_2O_2 reactants were examined in a lateral architecture. As depicted in Fig. 1b, current–voltage characteristics of the $Ag/SnO_x/Ag$ devices display a linear response for all SnO_x films. The H_2O-derived SnO_x film exhibits the lowest electrical conductivity, while the pure H_2O_2-based SnO_x film shows the highest electrical conductivity. The electrical conductivities of two H_2O/H_2O_2-converted SnO_x films with different combined cycles fall between them. Additionally, Fig. S1 shows that the H_2O_2-derived SnO_x film has a smaller optical absorption tail than pure H_2O-derived SnO_x film, indicating a reduction in the density of defect states present in the energy bands of the H_2O_2-derived SnO_x film, which contributes to the improved electrical conductivity of bulk films.[38] Additionally, the presence of these gap states is confirmed at the SnO_2 surface/interface and further revealed to be Sn 5s lone pairs by the Al K_α XPS valence band spectra, as shown in Fig. S2a.[39,40] Band energy diagrams of two types of SnO_x films were constructed by combining UV-vis absorption spectroscopy with ultraviolet photoelectron spectroscopy (UPS) (Fig. S2b and c). The results suggest that the Fermi level moves closer to the conduction band minimum (CBM) for the H_2O_2-derived SnO_x film, indicating the enhanced n-type doping behavior (Fig. S2d). Next, the efficacy of varying reactants-derived ALD SnO_x films as ETLs was explored based on single-junction halide perovskite solar cells (SPVKs) with a structure of $ITO/NiO_x/Me$-$4PACz/Al_2O_3/GABr/$ 1.81 eV $Cs_{0.3}FA_{0.7}Pb(I_{0.6}Br_{0.4})_3/GABr$:F-$PEAI/C_{60}/SnO_x/Ag$. Fig. 1c depicts the current–voltage (J–V) characteristics of these devices, while Table S1 summarizes their corresponding device parameters. Compared to the control devices with pure H_2O-converted SnO_x, which have an average PCE of 15.11%, both devices combined with two different H_2O/H_2O_2-converted SnO_x films deliver improved device performance, along with the enhanced J_{sc} and fill factor (FF), ascribing to the improved electrical properties of these films. Particularly, the optimal SPVKs with H_2O (70 cycles)/ H_2O_2 (70 cycles) SnO_x film achieve a hero efficiency of 16.67% with a J_{sc} of 16.79 mA cm^{-2}, a V_{oc} of 1.26 V, along with an FF of 78.66%. It is noteworthy that the H_2O/H_2O_2-converted SnO_x film with a larger number of H_2O_2 cycles (110 cycles) shows a tendency towards a slightly reduced performance of 15.99%. We further underline the relevance of processing a thin H_2O-derived SnO_x layer beneath the H_2O_2 one. Despite the better n-type character of pure H_2O_2-derived SnO_x films, corresponding SPVKs exhibit a significantly reduced performance of 12.42%, caused by a massive FF loss (61.88%) and a remarkable V_{oc} loss (1.22 V), likely due to the degradation effect of C_{60} and/or perovskite film from the diffusion of H_2O_2 and/or direct exposure to H_2O_2 atmosphere. These results demonstrate that a properly thick H_2O-converted SnO_x film is beneficial in protecting the underlying sensitive layers prior to depositing a H_2O_2-derived SnO_x film. The integrated J_{sc} values from external quantum efficiency (EQE) measurements are consistent with those from J–V scans performed under the AM 1.5G solar simulator, depicted in Fig. 1d. The statistical distributions of these device performances are illustrated in Fig. 1e, demonstrating excellent reproducibility. Accordingly, the optimized H_2O/H_2O_2 (70/70 cycles)-converted ALD SnO_x film was chosen for the following experiments.

Photovoltaic performance of P–O TSCs

To explore the efficacy of the optimized ICL based on $H_2O/$ H_2O_2-derived SnO_x in a tandem configuration, a device stack of $ITO/NiO_x/Me$-$4PACz/Al_2O_3/GABr/1.81$ eV $Cs_{0.3}FA_{0.7}Pb(I_{0.6}Br_{0.4})_3/$ $GABr$:F-$PEAI/C_{60}/SnO_x/PEDOT$:PSS/OSC/PDINN/Ag was built, as shown in Fig. 2a. A cross-sectional scanning electron microscopy (SEM) image of the fresh tandem cells shows the intact multiple-layer structure, which suggests that the SnO_x layer reliably protects the underlying WBG perovskite and C_{60} layers from damage by the subsequent spin-coating layers, including the processing of a water-based PEDOT:PSS layer. For comparison, the H_2O-derived SnO_x-based ICL is used for the fabrication of the control P–O TSCs. Electrical and optical properties of ICLs are critical parameters to determine the performance of TSCs. Fig. S3 and Fig. 2b demonstrate that the optimal ICL, the combined H_2O/H_2O_2-derived SnO_x film, shows slightly higher transmittance in the UV range and significantly improved vertical conductivity in comparison to the control ICL. Additionally, compared to the control pure H_2O-converted $SnO_x/PEDOT$:PSS-based device which displays a curved J–V curve, the H_2O/H_2O_2-processed $SnO_x/PEDOT$:PSS sample exhibits improved quasi-ohmic contact, suggesting the formation of a more favourable interface contact and enhanced electrical transport properties. Next, the efficacies of these two ICLs were evaluated in the P–O TSCs by combining a highly efficient ternary organic absorber, PM6: L8BO:BTP-eC9, as the rear OSC sub-cell. The detailed chemical structures of the used organic semiconductors, the J–V curves, and EQE spectra of p–i–n single-junction ternary OSCs combining PEDOT:PSS as the hole transporting layer and PDINN as the ETL are depicted in Fig. S4. The corresponding device performance parameters are summarized in Table S2, showing an average PCE of 17.47%. Fig. 2c presents the J–V curves of the perovskite-ternary (P-T) TSCs with H_2O-derived SnO_x and H_2O-/H_2O_2-derived SnO_x based ICLs, respectively. The corresponding photovoltaics parameters are summarized in Table S3. By combining with the PM6:L8BO:BTP-eC9 OSC ternary rear sub cell, the control tandem device yields a PCE of 21.75%, with a J_{sc} of 13.96 mA cm^{-2}, a V_{oc} of 2.07 V, and an FF of 75.26%. In contrast, the target tandem device employing H_2O/H_2O_2-processed SnO_x-based ICL delivers an improved PCE of 23.53%, along with a J_{sc} of 14.58 mA cm^{-2}, a V_{oc} of 2.08 V, and an FF of 77.58% under the reverse scan, and their corresponding JV curves exhibit negligible hysteresis effect. The target P-T TSC shows the main improvement in J_{sc} and FF. Next, a small amount of [70]PCBM was added to the ternary photo absorber to optimize the morphology of the rear OSC layer, enabling balanced charge transport and reduced nonradiative recombination, which lead to overall improved device parameters (Fig. S4 and Table S2).[42] Accordingly, the tandem involving the quaternary OSC achieves an impressive average PCE of 25.12%, with a notably improved J_{sc} of 15.38 mA cm^{-2}, a full V_{oc} of 2.11 V, and an FF of 77.40% (Fig. 2d). Notably, the significant enhancement in J_{sc} value of the perovskite-quaternary OSC TSC (P-Q TSC) is attributed to the combined effects of morphological optimization of the
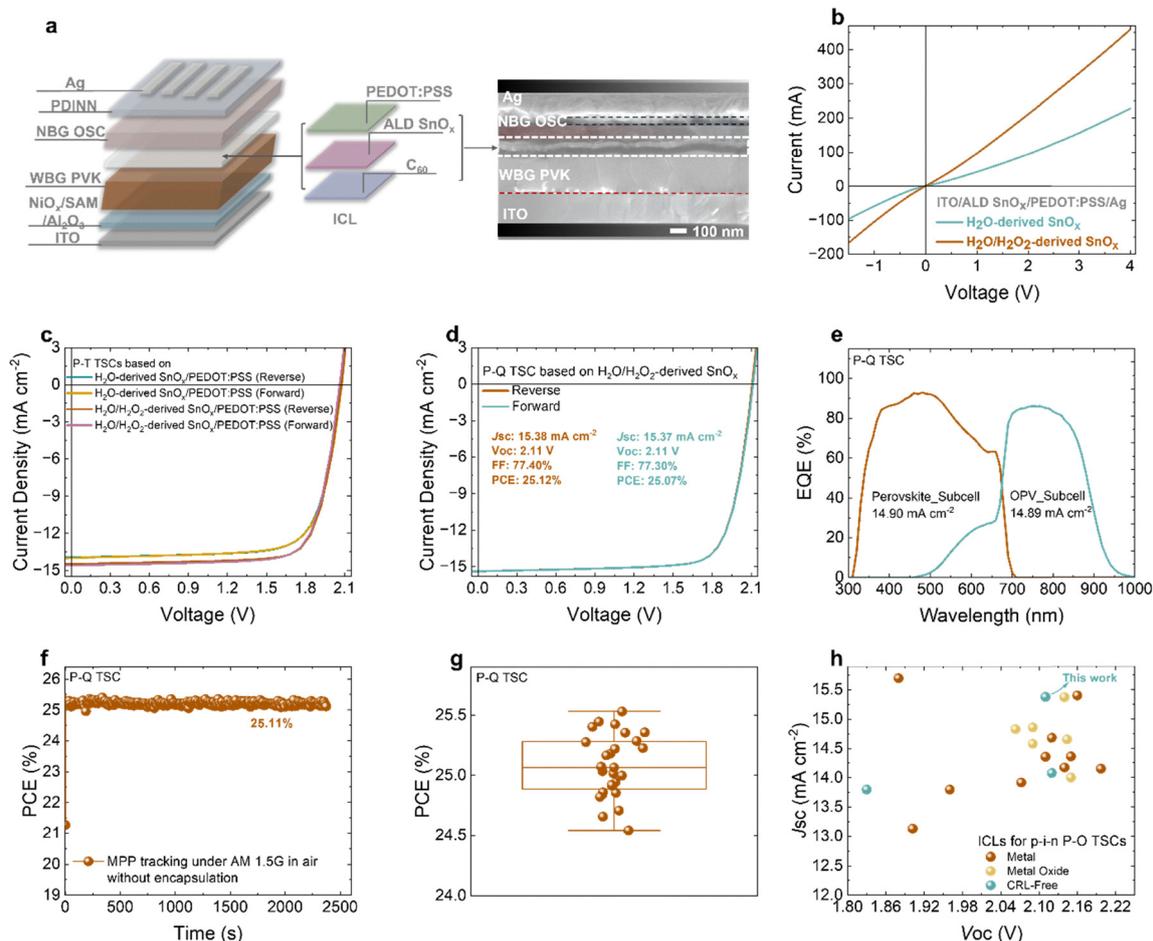
Fig. 2 Device architecture and performance of PO-TSCs. (a) Schematic diagram showing the p–i–n perovskite/organic TSCs and the corresponding cross-sectional SEM diagram. (b) J–V characteristics of the diode devices with the structure of ITO/H_2O-derived and H_2O-derived/H_2O_2-derived SnO_x/PEDOT:PSS/Ag. (c) J–V characteristics of P-Q TSCs with H_2O-derived SnO_x and H_2O-derived/H_2O_2-derived SnO_x-based ICLs, respectively. (d) and (e) J–V characteristics and the EQE spectra of P-Q TSC based on H_2O-derived/H_2O_2-derived SnO_x based ICLs with reverse and forward scanning directions. Self-adhesive anti-reflection films were used in the measurement of P-Q TSCs. (f) Stabilized PCE of the P-Q TSCs with H_2O-derived/H_2O_2-derived SnO_x ICL. (g) Statistical data of 28 P-Q TSCs measured with a reverse J–V scanning direction. (h) J_{sc} evolution *versus* V_{oc} of P-Q TSCs with various ICLs with or without extra CRLs. A more detailed summary can be found in Table S4.

quaternary rear OSC and reduced optical loss from the use of an anti-reflection film during the JV measurement. The perovskite-quaternary OSC-based TSC (P-Q TSC) displays excellent current matching between the front and rear sub-cells, as estimated from the integrated EQE spectrum (Fig. 2e). Moreover, the optimal P-Q TSC exhibits a stabilized steady power output of 25.11% (Fig. 2f). The performance statistics of P-Q TSCs verify the advantage of the ICL with H_2O-derived/H_2O_2-processed SnO_x for highly efficient P-Q TSCs (Fig. 2g and Fig. S5). Additionally, Fig. S6 highlights the unipolar electron transport property of H_2O-/H_2O_2-derived SnO_x as evidenced by a C_{60}/H_2O-derived and H_2O_2-derived SnO_x ICL, yielding a tandem performance of only 11.41%. Fig. 2h illustrates the J_{sc} evolution *versus* V_{oc} of state-of-the-art P-Q TSCs incorporating different kinds of ICLs with or without extra CRLs. This comparison highlights the significance of the optimal ICL architecture in minimizing optical and electrical losses.

Operational device stability of P–O TSCs

Both WBG halide perovskites and organic NFA-based OSCs are known to suffer from their respective leading degradation mechanisms. OSCs are prone to so-called burn-in effects, which are either correlated with a microstructure instability or spectrally sensitive degradation mechanism. WBG perovskite devices are susceptible to reactions between metal electrodes and mobile halide species, which can induce electrode corrosion and broad tail states in the perovskite layer, respectively.[43–45] The configuration of the P–O tandem device structure is speculated to offer a unique opportunity to mitigate or even to resolve these leading degradation mechanisms. On the one hand, capping the perovskite layer with the finely tuned organic semiconductor absorber layer, in combination with a well-designed of the ICL, can block bi-directional diffusion of halide ions and electrode ions and thus prevent corrosion of the top metal electrode, which is Ag in our case. On the other hand, the optical filter behavior of the perovskite front

cell, absorbing all high-energy radiation below 600 nm, is expected to stabilize the OSCs from spectrally sensitive degradation.[25,26] Thus, we designed a comparative experimental campaign, allowing us to side-by-side follow operational stability evolution for the respective single-junction half cells *versus* their tandem configuration. First, long-term light operational stability of the single-junction quaternary PM6:L8BO:BTP-eC9:[70]PCBM OSCs (SQOSCs) and the WBG SPVKs, as well as the corresponding P-Q TSCs combined with the optimal H_2O/H_2O_2-derived SnO_x-based ICL was evaluated, where unencapsulated devices were subjected to continuous MHL illumination with stabilized power-output tracking.[46] These unsealed devices without an extra UV filter were subjected to continuous illumination from MHL with power-output tracking. Fig. 3a and Fig. S7 illustrate that both SPVKs and SQOSCs only preserve 52.83% and 80.49%, respectively, of their respective initial efficiency under short-circuit mode, while the target tandem devices maintain 91.68% of their original performance after 1000 hours under short-circuit mode (Fig. 3a). This result strongly highlights the remarkable opportunity of the P–O tandem configuration in boosting device stability beyond both investigated single-junction counterparts. It is worth pointing out the tandem's temporal behavior under continuous operation is primarily governed by that of the perovskite sub-cell. Additionally, the lifetime reproducibility of the tandem devices was studied in different experimental runs and overall was found to be excellent (Fig. S8 and S9). Additionally, the stability of the tandem device was investigated under open-circuit

conditions with continuous illumination from the MHL illumination, retaining nearly 90% of its initial efficiency after aging near 1000 hours (Fig. S10). Besides, it is noted that the SPVKs with an additional annealing-treated PEDOT:PSS polymer film on top demonstrate to a slower degradation rate compared to the control SPVKs (Fig. S11).[47] This suggests that while the additional thin PEDOT:PSS polymer film can delay ion diffusion, it cannot fully prevent it due to its limited thickness, implying the crucial role of organic semiconductor layer in suppressing the ion diffusion in the tandem configuration.

We next turn our attention to whether fatigue behavior of perovskite-based devices can be mitigated by the P–O tandem configuration, which can be most relevantly investigated under day/night cyclic operation. Under these conditions, perovskites often exhibit degradation during the day, recovery during the night (Type I) and/or degradation during the night, recovery during the day (Type II), which depends on the status of device degradation during a cycle.[46,48,49] To maximize the simulation of the diurnal condition, we further conducted 12-hour day/12-hour night cycling aging test on SPVKs, SOSCs, and P–O tandem devices following the "International Summit on Organic Photovoltaic Stability LC protocol" (ISOS-LC).[46] Fig. S12 shows that SQOSCs exhibit no such fatigue behavior. As displayed Fig. 3b and Fig. S13, the WBG SPVKs display 33% performance loss, while the target tandem devices show marginal degradation after 61 aging cycles. The PCE evolution of SPVKs and P-Q TSCs in the representative cycles is further depicted in Fig. 3c. In the case of SPVKs, which demonstrate evident fatigue behavior, the PCE initially
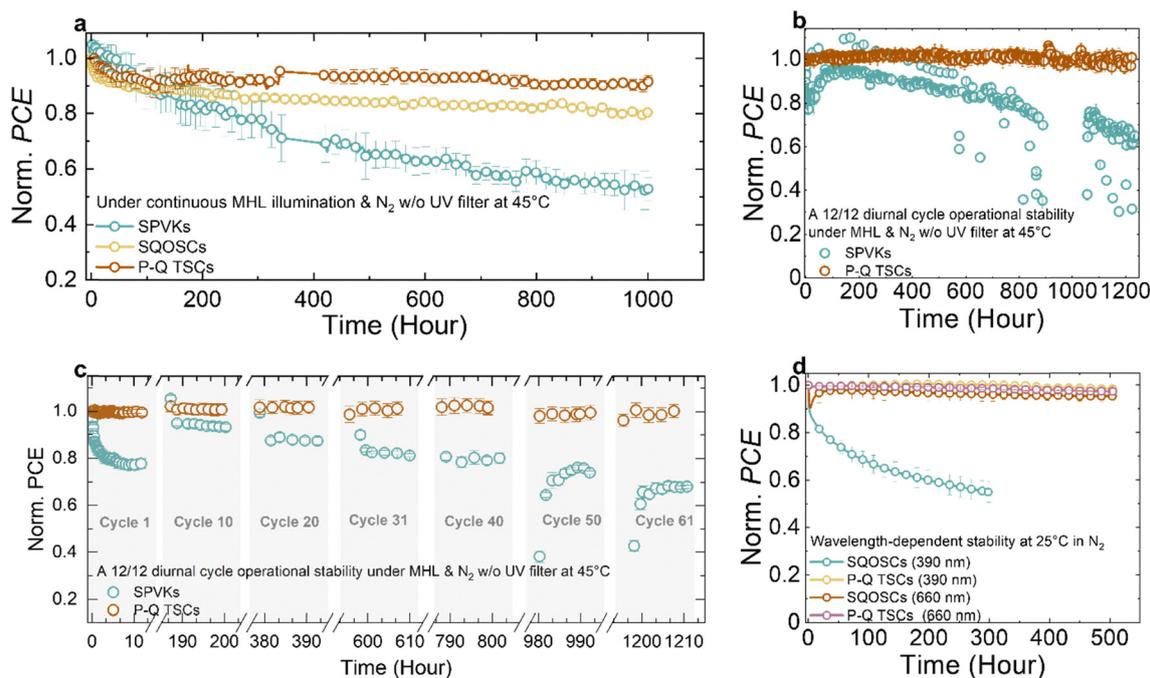

Fig. 3 Long-term device stability evaluation of P-Q TSCs. (a) Evolution of the normalized power output of unencapsulated SQOSCs, SPVKs, and P-Q TSCs under continuous MHL light irradiation and stabilized power-output tracking in a nitrogen flow. The stability of the P-Q TSCs was represented by the averaged data shown in Fig. S8. (b) and (c) Simulating tracking over a 12/12-hour diurnal cycle operation for the SPVKs and P-Q TSCs. (d) Evolution of normalized power output of SOSCs and P-Q TSCs illuminated under 390 nm (5 mW cm^{-2}) and 660 nm (100 mW cm^{-2}) monochromatic sources in a nitrogen flow.

decreases under illumination and recovers in the dark at the early cycles. The devices exhibit a noticeable "burn-in" effect, losing 22% of their PCE in the first cycle, mainly due to the obvious decrease in FF and V_{oc} with a minor contribution of J_{sc} loss within the first few hours (Fig. S14),[50] while a full PCE restoration of the SPVKs is observed during the night, but followed by further degradation upon reillumination in the first 20 cycles, likely due to the light-induced ion migration.[48] Interestingly, the PCE dynamics of SPVKs shifts to Type II diurnal behavior in the later degradation stage (e.g. Cycle 50), indicating the emergence of new degradation mechanisms and the interplay among superimposed factors.[49] Both PCE restoration and degradation are observed in the aging operation, implying that reversible and irreversible degradation mechanisms co-exist in the WBG SPVKs.[48] Notably, both the PCE restoration rate and extent of SPVKs reduce gradually along with consecutive diurnal cycle, suggesting the increase of irreversible degradation mechanisms, such as irreversible migration of ionic species within the devices and corrosion at the metal electrode.[43,44,49,51] In contrast, the stability of tandem devices remains unchanged throughout the test, exhibiting extraordinarily enhanced anti-fatigue stability under cyclic light/dark stress conditions. This result underlines the successful stabilization of the perovskite half-cell in a tandem configuration with capped polymer organic layers on top. It is noted that the target tandem devices still operate at 96.80% of their initial performance, presenting literally burn-in free or light-soaking free operation even after a long light/dark cycle operation of 2067 hours (i.e., 86 cycles). This represents one of the best anti-fatigue stabilities for perovskite-based devices (Fig. S15) so far. The overall stability results shown in Fig. 3a–c confirm the unique opportunity to stabilize perovskite cells by integrating them into a tandem configuration with a combination of the ICL and a polymer organic back sub-cell.

Preventing spectrally induced degradation via the perovskite layer

Having established that the tandem configuration indeed shows superior operational stability as compared to the respective single-junction cells, we turn our attention to the underlying mechanism enhancing the stability of the organic sub-cell. In our tandem configuration, a 1.81 eV-PVK sub-cell with an absorption edge at approximate 710 nm is used. Our previous studies have shown that most organic solar cells demonstrate a dramatic increase in operational stability when protected from light below 600 nm.[35] In the tandem, the perovskite sub-cell is expected to efficiently filter out the damaging high-energy light for the rear organic sub-cell and allow it to operate stably in the benign absorption region above 600 nm.[2,34] Therefore, to evidence the stabilization mechanism of the organic sub-cell in a tandem configuration, we operated the respective SQOSCs and tandem-junction devices under two monochromatic LEDs peaked at 390 nm and 660 nm, respectively. Fig. 3d and Fig. S16 demonstrate that both SQOSCs and P-Q TSCs maintain nearly unchanged performance at 660 nm irradiation with a 1-sun equivalent intensity, showing consistent behavior with the reported literature.[34] Nevertheless, when

illuminated under a high-energy light at 390 nm (5 mW cm^{-2}), the SQOSCs degrade pronouncedly, while the corresponding tandem cells demonstrate a negligible performance loss, showcasing the excellent protective effect of the perovskite layer for the organic components.

Blocking bi-directional migration pathway via dense organic layers

Having demonstrated that the two sub-cells stabilize each other mutually, we turn to the question of how the polymer organic half-cell manages to stabilize the halide perovskite half-cell. It has been well-documented that the bi-directional migration of halides or halogen species and silver causes irreversible chemical corrosion to the electrodes and the depletion of halides in the perovskite layers by forming insulating silver halides or defect states at the bulk or interface of the perovskite film, limiting the long-term operational stability of SPVKs.[44,52,53] Our P-Q tandem architecture exhibits extraordinary stability under illumination, indicating the effective suppression of bi-directional ion migration of the perovskite and silver electrode within the devices. To verify the effectiveness of the organic capping layer in suppressing the bi-directional ion migration of perovskite and Ag electrode during device operation, we prepared cross-sectional lamellae from both freshly-prepared and aged (1000 hours of continuous operation) samples of SPVKs and the target P-Q TSCs (cf. materials and methods) and conducted scanning transmission electron microscopy (STEM) and energy dispersive X-ray spectroscopy (EDXS) to straightforwardly shed light on the superior long-term stability mechanism of P-Q TSCs over the single-junction perovskite device. Fig. 4a and Fig. S17 depict that perovskite-related elements, such as Br, I, and Pb, are homogenously distributed within the perovskite layer of the fresh SPVK sample. This contrasts sharply with the elemental distribution observed in the SPVK sample after 1000 hours of light-induced degradation. As shown in Fig. 4b and Fig. S18, a massive accumulation of Br is revealed at the Ag electrode, accompanied by noticeable traces of I and even a small fraction of Pb. These findings clearly evidence that the thermally-evaporated C_{60} film and the 20 nm-thick ALD SnO$_2$ layer fail to act as effective barriers for the diffusion of Br and I, which are eventually scavenged by Ag ions to form metastable or stable metal halide complexes.[44] Furthermore, we note that in the elemental signal profiles, the Br signal is much higher than that of I. The complementary amount of Br relative to I and Pb signals at the Ag layer indicates that the diffusivity of Br$^-$ ions across the C_{60} layer toward the Ag electrode after decomposition is higher than that of the I$^-$ ions. Interestingly, we also observed a few distinct flocculent-like features, vertically distributed in certain regions in the C_{60} layer, appearing as the bright flocculent-like features in the HAADF-STEM images of the aged SPVK device (Fig. 4b and Fig. S19b), suggesting the presence of heavier elements in these regions. To gain further insights into the flocculent-like features within the aged C_{60} film, we examined the sum EDXS spectra from a region of flocculent-like feature (color coded and marked into area #1)

This journal is © The Royal Society of Chemistry 2026

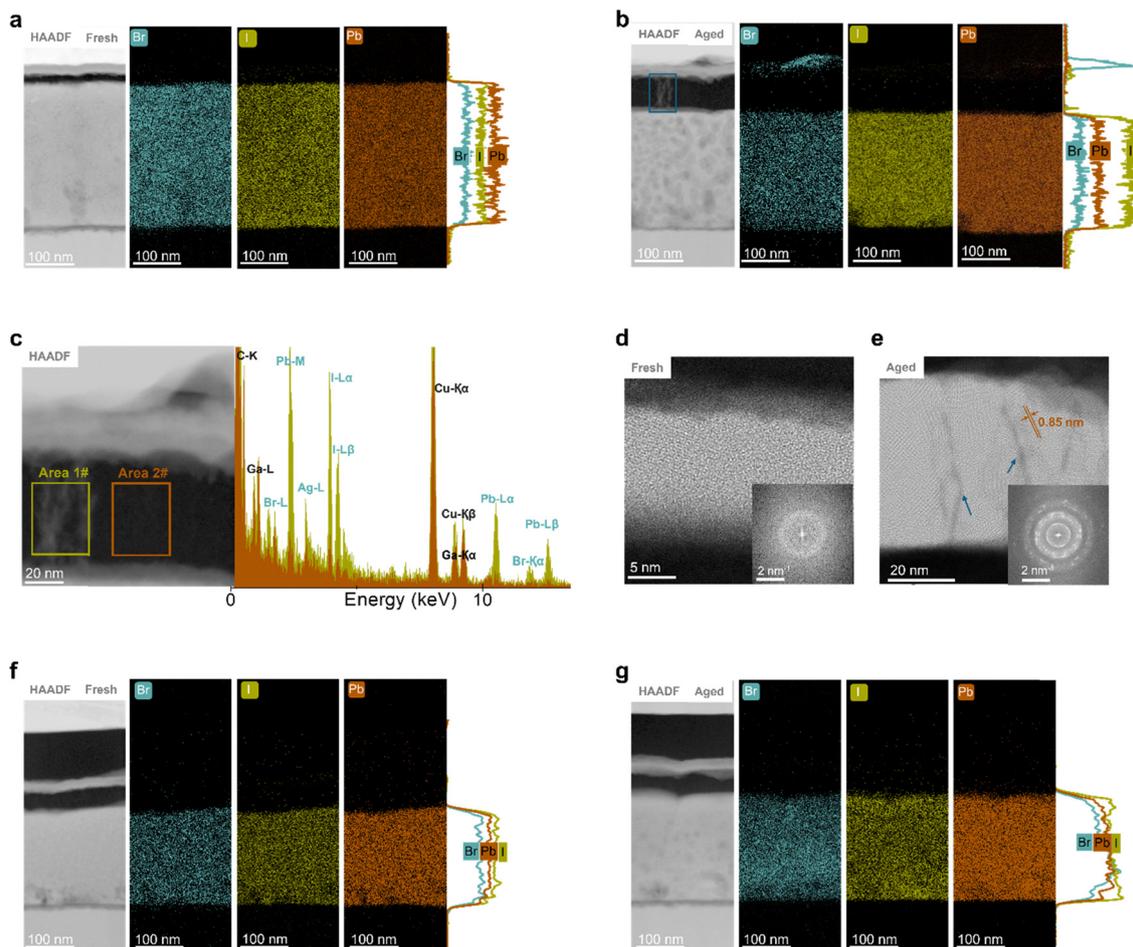Energy Environ. Sci., 2026, 19, 1137–1147 | 1143

Fig. 4 Cross-sectional STEM and EDXS characterization. (a) and (b) Cross sectional STEM-HAADF images and the corresponding EDXS maps of Br, I, and Pb of fresh and aged SPVK, respectively. (c) The zoom-in area of flocculent-like features in the aged C_{60} film and the corresponding EDX spectra extracted from two marked areas, *i.e.*, area #1 from flocculent-like features region and area #2 from its neighbouring region without the flocculent-like feature as seen from the corresponding STEM-HAADF image. Noted that the y axis scale of the EDX spectrum represents the counts of X-ray photons. (d) and (e) STEM bright-field images of C_{60} films of freshly prepared and aged SPVK devices, respectively, with the FFT images as insets. (f) and (g) Cross-sectional STEM-HAADF images and the corresponding EDXS maps of Br, I, and Pb of fresh and aged P-Q TSCs, respectively.

and compare it with a region in its direct vicinity (color coded and marked into area #2), as shown in Fig. 4c. The EDXS spectra from area 1# and area 2# clearly reveals the existence of Pb and I with traces of Br and Ag. The detection of Ag–L signal within the C_{60} layer demonstrates the deep inward diffusion of the Ag into the perovskite layer during the ageing operation under illumination. Particularly in area 1#, where distinct flocculent features are visible, the signals of both perovskite-related and Ag species are significantly stronger than those in area 2#. Together with the corresponding EDXS maps (Fig. S20), these results support the conclusion that the grain boundaries in the crystalline C_{60} films act as preferential, faster diffusion channels for ion migration during the solar cell operation. One hypothesis is that the C_{60} film undergoes recrystallization during ageing operation, leading to the development of these structural features. To further verify this point, we took a close look into the C_{60} layer using the phase contrast scanning transmission electron microscopy (STEM) bright-field (BF) imaging, which allowed us to best reveal the structure

changes before and after ageing treatment. Our analysis reveals a clear difference in the crystallinity levels between the fresh and aged C_{60} layers. For the C_{60} film in the fresh SPVK device, the contrast of image in Fig. 4d, along with the halo ring in fast Fourier transform (FFT) image demonstrate a basically amorphous phase. Ordered domains are occasionally observed with very weak lattice contrast. In contrast, the morphology of the C_{60} layer in the aged SPVK sample is characterized by different crystalline domains (Fig. 4e). The corresponding FFT image clearly shows sharp spots from lattices arranged into at least 5 discernable rings of different radii, suggesting higher degree of crystallinity, whereas the ring shape of the FFT image suggests the random orientation of crystalline C_{60} film in imaged field of view in the aged film. The recrystallization of C_{60} during aging may arise from the synergistic effects of localized photothermal heating at the perovskite/C_{60} interface, energy transfer from injected "hot" carriers, and localized photothermal heating. The dark-trace, flocculent-like features in STEM-BF images (Fig. 4e), representing the diffusion

channels of the Pb, Br, I, and Ag, appear to follow grain boundaries of C_{60} crystal domains, suggesting a grain boundary mediated diffusion mechanism. Having established the C_{60} layer as an active element in regulating ion diffusion in the aged SPVK, we come back to the presumed suppression of ion diffusion in tandem cells. As expected, the tandem device demonstrates an entirely different behavior during the identical aging operation condition. Fig. 4g and Fig. S22, reveal that the characteristic mobile ions, Br, I, and Pb, remain largely "frozen" in the halide perovskite layer of the aged tandem device. Despite the slight ion redistribution within the bulk, the aged tandem device still maintains its perovskite structure and typical grain sizes, with the elemental distribution of mobile ions remaining similar to that of the fresh tandem device (Fig. 4f and Fig. S21). Additionally, while a few flocculent-like features are present in the aged tandem sample, they are significantly sparser compared to those in the SPVK sample (Fig. S19b and d), suggesting the efficiently suppressed occurrence of ion migration. Furthermore, no detectable signals of mobile perovskite ions were observed in either the organic layer or the Ag top electrode. By further combining the device stability results of P–O tandem devices and SPVKs with the complete ICL (Fig. 3a and Fig. S11), it suggests that the capped polymer organic sub-cell serves as a primary permeation barrier, effectively preventing electrode corrosion caused by outward ion diffusion from the perovskite layer while also blocking the intrusion of Ag ions into the perovskite layer.[54]

Conclusions

In this work, we demonstrate outstanding performance and stability for hybrid P–O TSCs utilizing an advanced CRL-free ICL with a structure of C_{60}/H_2O-derived and H_2O_2-derived ALD SnO_x/PEDOT:PSS. The ICL confers both excellent electrical, optical properties, and form a low-loss quasi-ohmic contact junction, which results in an averaged PCE of 25.12% (with a champion PCE of 25.53%) for P–O TSCs. Importantly, we provide critical insights into the enhanced stability of high-performance hybrid P–O TSCs. A notable finding is that the significant harmful bi-directional ion migration of the perovskite-related halide species and Ag ions occurs along the grain boundaries, which are formed in the C_{60} film of single perovskite devices, resulting from recrystallization during ageing operation. Notably, the tandem configuration demonstrates unique stability advantages in efficiently regulating the ion interdiffusion by the integration of organic semiconductor layers, thus creating an inherently "self-stabilizing" system: the organic layers stabilize the perovskite sub-cell by suppressing ion diffusion-induced degradation, while the perovskite layer protects the organic sub-cell from spectral sensitivity-induced degradation. The simultaneous dual stabilization protection mechanism ensures exceptional long-term operational photostability for P-Q TSCs, reserving over 91% of their initial performance after 1000 hours of continuous light exposure under MHL at 45 °C; additionally, it enables negligible fatigue

behavior after 86 operational 12/12-hour diurnal cycles (2067 hours), remarkably surpassing the stability of both single-junction cells. This work fully demonstrates the potential of P–O tandem configuration with inherent stability, alongside improved efficiency, offering a compelling prospect for intensifying future research into P–O tandem technologies. Additionally, uncovering the limitations of the commonly used C_{60} film offers valuable insights for exploring more durable interface materials for future advancements in both perovskite-based single-junction and tandem architectures.

Author contributions

C. L. and K. Z. conceived the idea of the work and designed the project. C. L., K. Z. and C. J. B. supervised the research. C. L. and K. Z. fabricated tandem devices. C. L. performed the optical and electrical characterizations, ALD processes, as well as device performance and stability measurements. X. Z., M. W., and E. S. performed FIB lamellae preparation, STEM, and EDXS measurements and greatly supported the analysis of these measurements. P. W. helped with the wavelength-dependent stability test. S. Q. measured SEM images. M. A., J. F., R. G. W., and M. B. performed and analyzed XPS and UPS measurements. J. E. and J. B. provided the ALD equipment support. Z. P. and Y. H. provided valuable assistance in stability data analysis by programing python script. T. H. provided the equipment support for the stability characterization. N. L., J. W., C. H. L., J. T., Z. P., and J. Z. provided valuable assistance in data analysis and curation. C. L. wrote the first draft of the manuscript. All the authors revised and approved the manuscript.

Conflicts of interest

There are no conflicts to declare.

Data availability

All data which support this study are included in the published Article and its supplementary information (SI). All experimental procedures is available in supplementary information. See DOI: **https://doi.org/10.1039/d5ee05397h**.

Acknowledgements

This journal is © The Royal Society of Chemistry 2026

Energy Environ. Sci., 2026, **19**, 1137–1147 | 1145

References

1 S. Wu, M. Liu and A. K. Y. Jen, Prospects and challenges for perovskite–organic tandem solar cells, *Joule*, 2023, **7**, 484–502.

2 K. O. Brinkmann, *et al.*, Perovskite–organic tandem solar cells, *Nat. Rev. Mater.*, 2024, **9**, 202–217.

3 M. Heydarian, *et al.*, Recent progress in monolithic two-terminal perovskite-based triple-junction solar cells, *Energy Environ. Sci.*, 2024, **17**, 1781–1818.

4 S. Tao, *et al.*, Absolute energy level positions in tin- and lead-based halide perovskites, *Nat. Commun.*, 2019, **10**, 2560.

5 D. P. McMeekin, *et al.*, A mixed-cation lead mixed-halide perovskite absorber for tandem solar cells, *Science*, 2016, **351**, 151–155.

6 M. A. Green, *et al.*, Solar cell efficiency tables (Version 66), *Prog. Photovolt.: Res. Appl.*, 2025, **33**, 725–810.

7 h (http://h)https://ttps://www.nrel.gov/pv/assets/images/cell-pv-eff-hybridtandems.jpg.

8 R. Wang, *et al.*, Prospects for metal halide perovskite-based tandem solar cells, *Nat. Photonics*, 2021, **15**, 411–425.

9 K. Xiao, *et al.*, All-perovskite tandem solar cells with 24.2% certified efficiency and area over 1 cm^2 using surface-anchoring zwitterionic antioxidant, *Nat. Energy*, 2020, **5**, 870–880.

10 R. Lin, *et al.*, Monolithic all-perovskite tandem solar cells with 24.8% efficiency exploiting comproportionation to suppress Sn(II) oxidation in precursor ink, *Nat. Energy*, 2019, **4**, 864–873.

11 Y. Jiang, *et al.*, Non-fullerene acceptor with asymmetric structure and phenyl-substituted alkyl side chain for 20.2% efficiency organic solar cells, *Nat. Energy*, 2024, **9**, 975–986.

12 C. Li, *et al.*, Organic solar cells with 21% efficiency enabled by a hybrid interfacial layer with dual-component synergy, *Nat. Mater.*, 2025, **24**, 1626–1634.

13 Z. Jia, *et al.*, Efficient near-infrared harvesting in perovskite–organic tandem solar cells, *Nature*, 2025, **643**, 104–110.

14 S. Wu, *et al.*, Redox mediator-stabilized wide-bandgap perovskites for monolithic perovskite–organic tandem solar cells, *Nat. Energy*, 2024, **9**, 411–421.

15 W. Chen, *et al.*, Monolithic perovskite/organic tandem solar cells with 23.6% efficiency enabled by reduced voltage losses and optimized interconnecting layer, *Nat. Energy*, 2022, **7**, 229–237.

16 X. Wang, *et al.*, Highly efficient perovskite/organic tandem solar cells enabled by mixed-cation surface modulation, *Adv. Mater.*, 2023, **35**, 2305946.

17 Z. Zhang, *et al.*, Suppression of phase segregation in wide-bandgap perovskites with thiocyanate ions for perovskite/organic tandems with 25.06% efficiency, *Nat. Energy*, 2024, **9**, 592–601.

18 K. O. Brinkmann, *et al.*, Perovskite–organic tandem solar cells with indium oxide interconnect, *Nature*, 2022, **604**, 280–286.

19 X. Jiang, *et al.*, Isomeric diammonium passivation for perovskite–organic tandem solar cells, *Nature*, 2024, **635**, 860–866.

20 X. Guo, *et al.*, Stabilizing efficient wide-bandgap perovskite in perovskite–organic tandem solar cells, *Joule*, 2024, **8**, 2554–2569.

21 H. Yang, *et al.*, Regulating charge carrier recombination in the interconnecting layer to boost the efficiency and stability of monolithic perovskite/organic tandem solar cells, *Adv. Mater.*, 2023, **35**, 2208604.

22 S. Jiang, *et al.*, Synergistic electrical and light management enables efficient monolithic inorganic perovskite/organic tandem solar cells with over 24% efficiency, *Energy Environ. Sci.*, 2024, **17**, 219–226.

23 B. Abdollahi Nejand, *et al.*, Scalable two-terminal all-perovskite tandem solar modules with a 19.1% efficiency, *Nat. Energy*, 2022, **7**, 620–630.

24 J. Tian, *et al.*, Overcoming optical losses in thin metal-based recombination layers for efficient n–i–p perovskite–organic tandem solar cells, *Nat. Commun.*, 2025, **16**, 154.

25 C. C. Boyd, *et al.*, Barrier design to prevent metal-induced degradation and improve thermal stability in perovskite solar cells, *ACS Energy Lett.*, 2018, **3**, 1772–1778.

26 S. Svanstrom, *et al.*, Degradation mechanism of silver metal deposited on lead halide perovskites, *ACS Appl. Mater. Interfaces*, 2020, **12**, 7212–7221.

27 Y. Dong, *et al.*, Interface reactive sputtering of transparent electrode for high-performance monolithic and stacked perovskite tandem solar cells, *Adv. Mater.*, 2024, **36**, 2312704.

28 Y. M. Xie, Q. Yao, H. L. Yip and Y. Cao, Influence of component properties on the photovoltaic performance of monolithic perovskite/organic tandem solar cells: sub-cell, interconnecting layer, and photovoltaic parameters, *Small Methods*, 2023, **7**, 2201255.

29 G. Xie, *et al.*, Phase Segregation and voltage loss mitigated highly efficient perovskite–organic tandem solar cells with a

1146 | *Energy Environ. Sci.*, 2026, **19**, 1137–1147

This journal is © The Royal Society of Chemistry 2026

simple ambipolar SnO$_x$ interconnecting layer, *Adv. Funct. Mater.*, 2023, **33**, 2308794.

30 H. Xu, *et al.*, Metal-free interconnecting layer for monolithic perovskite/organic tandem solar cells with enhanced outdoor stability, *ACS Appl. Energy Mater.*, 2022, **5**, 14035–14044.

31 X. Zhou, *et al.*, Suppressing nonradiative losses in wide-band-gap perovskites affords efficient and printable all-perovskite tandem solar cells with a metal-free charge recombination layer, *ACS Energy Lett.*, 2022, **8**, 502–512.

32 Z. Yu, *et al.*, Simplified interconnection structure based on C$_{60}$/SnO$_{2-x}$ for all-perovskite tandem solar cells, *Nat. Energy*, 2020, **5**, 657–665.

33 J. W. Elam, *et al.*, Atomic layer deposition of tin oxide films using tetrakis (dimethylamino) tin, *J. Vac. Sci. Technol., A*, 2008, **26**, 244–252.

34 P. Weitz, *et al.*, Revealing photodegradation pathways of organic solar cells by spectrally resolved accelerated lifetime analysis, *Adv. Energy Mater.*, 2022, **13**, 2202564.

35 P. Weitz, *et al.*, Photodegradation of organic solar cells under visible light and the crucial influence of its spectral composition, *ACS Appl. Mater. Interfaces*, 2024, **16**, 36667–36677.

36 T. Liu, *et al.*, Photochemical decomposition of Y-series non-fullerene acceptors is responsible for degradation of high-efficiency organic solar cells, *Adv. Energy Mater.*, 2023, **13**, 2300046.

37 S. U. Lee, H. Park, H. Shin and N. G. Park, Atomic layer deposition of SnO$_2$ using hydrogen peroxide improves the efficiency and stability of perovskite solar cells, *Nanoscale*, 2023, **15**, 5044–5052.

38 N. Ren, *et al.*, 50 °C low-temperature ALD SnO$_2$ driven by H$_2$O$_2$ for efficient perovskite and perovskite/silicon tandem solar cells, *Appl. Phys. Lett.*, 2022, **121**, 033502.

39 L. A. Jones, *et al.*, Sn 5s^2 lone pairs and the electronic structure of tin sulphides: a photoreflectance, high-energy photoemission, and theoretical investigation, *Phys. Rev. Mater.*, 2020, **4**, 074602.

40 M. Weidner, Fermi level determination in tin oxide by photoelectron spectroscopy: relation to optoelectronic properties; band bending at surfaces and interfaces; modulation doping, PhD thesis, TU Darmstadt, 2016.

41 B. Yu, *et al.*, Impermeable atomic layer deposition for sputtering buffer layer in efficient semi-transparent and tandem solar cells via activating unreactive substrate, *Adv. Mater.*, 2023, **35**, 2202447.

42 K. N'Konou, S. Y. Kim and N. Y. Doumon, Multicomponent organic blend systems: a review of quaternary organic photovoltaics, *Carbon Energy*, 2024, **6**, e579.

43 X. Ren, *et al.*, Mobile iodides capture for highly photolysis- and reverse-bias-stable perovskite solar cells, *Nat. Mater.*, 2024, **23**, 810–817.

44 S. Wu, *et al.*, A chemically inert bismuth interlayer enhances long-term stability of inverted perovskite solar cells, *Nat. Commun.*, 2019, **10**, 1161.

45 W. Tress, *et al.*, Interpretation and evolution of open-circuit voltage, recombination, ideality factor and subgap defect states during reversible light-soaking and irreversible degradation of perovskite solar cells, *Energy Environ. Sci.*, 2018, **11**, 151–165.

46 M. V. Khenkin, *et al.*, Consensus statement for stability assessment and reporting for perovskite photovoltaics based on ISOS procedures, *Nat. Energy*, 2020, **5**, 35–49.

47 C. Liu, *et al.*, A cross-linked interconnecting layer enabling reliable and reproducible solution-processing of organic tandem solar cells, *Adv. Energy Mater.*, 2020, **10**, 1903800.

48 M. V. Khenkin, *et al.*, Dynamics of photoinduced degradation of perovskite photovoltaics: from reversible to irreversible processes, *ACS Appl. Energy Mater.*, 2018, **1**, 799–806.

49 L. Jiang, *et al.*, Fatigue sStability of CH$_3$NH$_3$PbI$_3$ Based Perovskite Solar Cells in Day/Night Cycling, *Nano Energy*, 2019, **58**, 687–694.

50 K. Domanski, *et al.*, Migration of cations induces reversible performance losses over day/night cycling in perovskite solar cells, *Energy Environ. Sci.*, 2017, **10**, 604–613.

51 Y. Zhang, *et al.*, Improved fatigue behaviour of perovskite solar cells with an interfacial starch-polyiodide buffer layer, *Nat. Photonics*, 2023, **17**, 1066–1073.

52 C. Gong, *et al.*, Silver coordination-induced n-doping of PCBM for stable and efficient inverted perovskite solar cells, *Nat. Commun.*, 2024, **15**, 4922.

53 P. Chen, *et al.*, Multifunctional ytterbium oxide buffer for perovskite solar cells, *Nature*, 2024, **625**, 516–522.

54 L. Shen, *et al.*, Ultrathin polymer membrane for improved hole extraction and ion blocking in perovskite solar cells, *Nat. Commun.*, 2024, **15**, 10908.

This journal is © The Royal Society of Chemistry 2026

Energy Environ. Sci., 2026, **19**, 1137–1147 | **1147**